

Statistical distribution of static stress resolved onto geometrically-rough faults

Jeremy Maurer  * 1

¹Geological Sciences and Geological and Petroleum Engineering, Missouri University of Science and Technology, Rolla, USA

Abstract The in-situ stress state within fault zones is technically challenging to characterize, requiring the use of indirect methods to estimate. Most work to date has focused on understanding average properties of resolved stress on faults, but fault non-planarity should induce spatial variations in resolved static stress on a single fault. Assuming a particular stochastic model for fault geometry (band-limited fractal) gives an approximate analytic solution for the probability density function (PDF) on fault stress that depends on the mean fault orientation, mean stress ratio, and roughness level. The mean stress is shown to be equal to the planar fault value, while deviations are described by substituting a second-order polynomial expansion of the stress ratio into the inverse distribution on fault slope. The result is an analytical expression for the PDF of shear-to-normal stress ratio on 2-D rough faults in a uniform background stress field. Two end-member distributions exist, one approximately Gaussian when all points on the fault are well away from failure, and one reverse exponential, which occurs when the mean stress ratio approaches the peak. For the range of roughness values expected to apply to crustal faults, stress deviations due to geometry can reach nearly 100% of the background stress level. Consideration of such a distribution of stress on faults suggests that geometric roughness and the resulting stress deviations may play a key role in controlling earthquake behavior.

Production Editor:
Gareth Funning
Handling Editor:
Pathikrit Bhattacharya
Copy & Layout Editor:
Ethan Williams

Signed reviewer(s):
Pierre Romanet

Received:
2 July 2023
Accepted:
17 May 2024
Published:
21 July 2024

1 Introduction

Fault stress is difficult to measure in the earth's crust and is affected by many factors, including slip both locally and on nearby faults, variations in material properties along faults, and geometric complexity. The distribution of prestress, i.e., stress prior to an earthquake mainshock rupture occurring, likely has a strong impact on both the rate and magnitude of earthquake ruptures that occur (Day, 1982; Oglesby, 2005; King and Nábělek, 1985; Fang and Dunham, 2013; Bruhat et al., 2016; Cattania and Segall, 2021; Dieterich et al., 2015; Dempsey et al., 2016; Maurer et al., 2020; Romanet et al., 2020). Geometric complexity in particular has been shown to affect the mechanics of slip on faults and may also impact the prestress (e.g., Duan and Oglesby, 2007; Fang and Dunham, 2013; Tal et al., 2018; Cattania and Segall, 2021). All faults present some degree of geometrical complexities, including at both long and small length scales (Power et al., 1987; Sagy et al., 2007; Candela et al., 2009, 2012; Brodsky et al., 2016; Thom et al., 2017; Zielke et al., 2017; Kirkpatrick et al., 2020; Tal et al., 2020). Geometry impacts the slip tendency and the evolution of stress during slip, through which it plays a role in controlling eventual earthquake size and characteristics (e.g., Oglesby, 2005; King and Nábělek, 1985; Fang and Dunham, 2013; Bruhat et al., 2016; Maurer et al., 2020). Obvious examples are restraining and releasing bends, which both act as barriers and as potential nucleation sites (e.g., Oglesby, 2005; King and Nábělek, 1985; Bhat et al., 2004; Duan and Oglesby, 2007; Ando and

Kaneko, 2018).

The distribution of pre-stress on faults has been explored in the context of the size distribution of seismicity (e.g., Andrews, 1980), with regards to fault slip during earthquake nucleation (Tal et al., 2018) and propagation (Dieterich et al., 2015; Dempsey and Suckale, 2016), and for induced seismicity, with regard to the maximum magnitude of induced events (Kroll and Cochran, 2021). Even for the same geometry, fault prestress has a strong impact on dynamic rupture outcomes (Tarnowski et al., 2022). Studies of dynamic earthquake rupture on rough faults has shown that roughness impacts ruptures in several ways. Dynamic simulations have showed that geometric roughness and the resulting stress variability has a strong impact on rupture size, speed, location, and even whether faults slip seismically or aseismically (e.g., Fang and Dunham, 2013; Bruhat et al., 2016; Tal et al., 2018; Allam et al., 2019). Fault prestress becomes heterogeneous over multiple earthquake cycles near branches in earthquake simulations (Duan and Oglesby, 2007), and in some cases earthquakes nucleate specifically due to stress concentrations resulting from geometric features such as restraining bends (Allam et al., 2019). Furthermore, fault roughness may induce slow slip and foreshocks due to normal stress variability occurring on faults that have orientations that vary from optimal along strike (Tal et al., 2018; Cattania and Segall, 2021). Earthquake cycle simulations incorporating roughness have shown that it has an important influence on individual ruptures and on the magnitude-frequency distribution of events, and that stress variability controls earthquake size over multiple

*Corresponding author: jmaurer@mst.edu

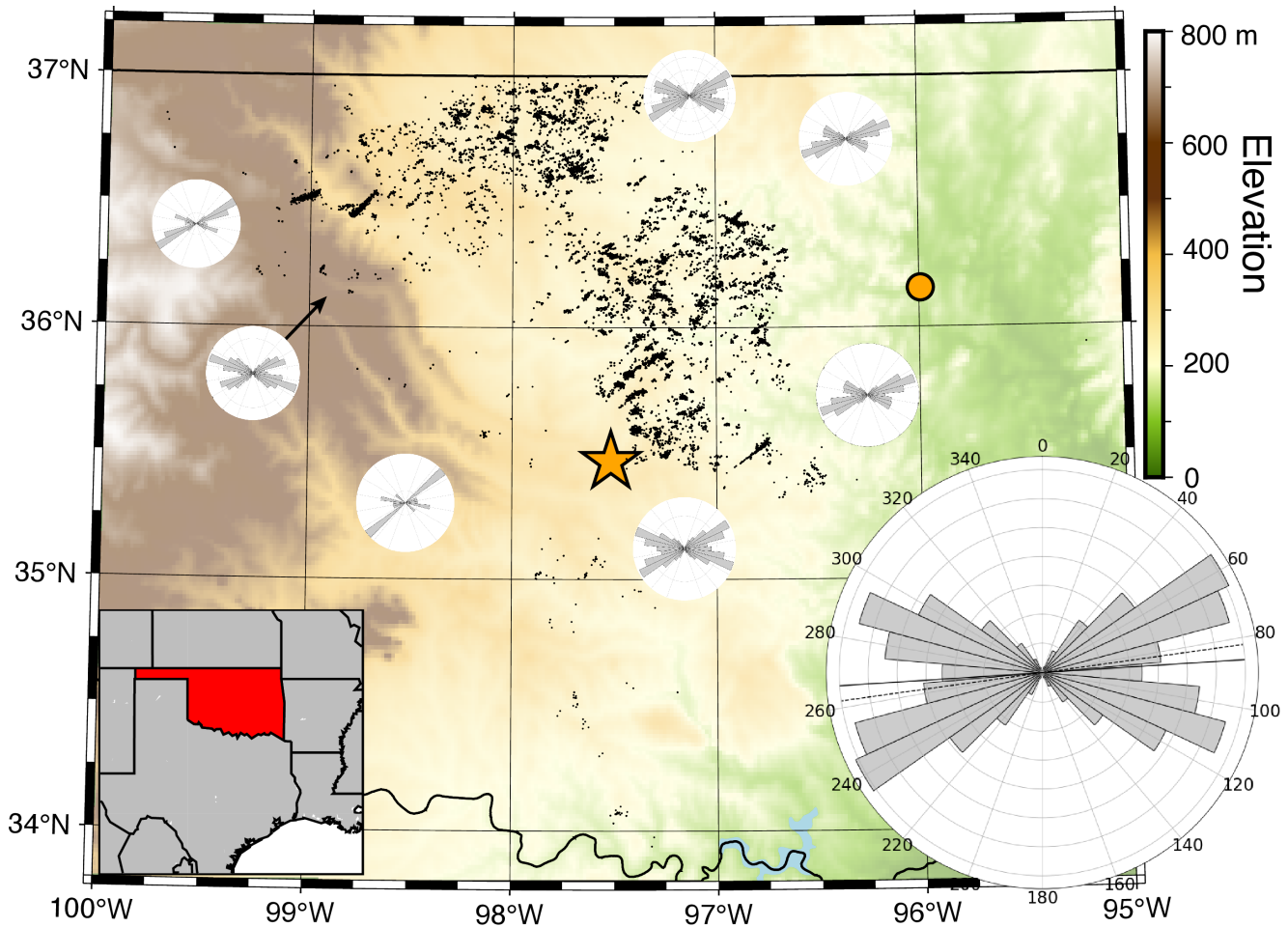


Figure 1 Seismicity (black dots) in Oklahoma from Schoenball and Ellsworth (2017). Rose diagrams show the orientations of fault segments inferred by Schoenball and Ellsworth (2017). Diagram for the entire region is shown in the lower right corner, while rose diagrams for each 1x1 degree cell are shown in each box or by arrows pointing to the appropriate box.

cycles (Heimisson, 2020). Observations of real earthquakes, such as El-Mayor Cucupah and Kaikoura, require mechanisms for both maintaining fault stability at high slip tendency and destabilizing faults with low slip tendency (Fletcher et al., 2016), which can only be accomplished through fault roughness. Taken together, these models and observations suggest that variability in fault prestress due to geometric roughness influences the location, timing and size of earthquakes, and that the interaction between fault geometry and fault loading will determine how ruptures propagate and earthquake cycles develop on faults.

A recent opportunity for learning more about *in situ* crustal stresses is induced seismicity. Observations of anthropogenically-induced earthquakes in relatively uniform stress conditions (e.g., induced seismicity in cratons) has shown that although fault orientations activated by fluid injection are generally seen to be consistent with the inferred regional stress field (Lund-Snee and Zoback, 2022), there are a range of orientations that activate, including some orientations well away from the regional mean SHmax direction (Schoenball and Ellsworth, 2017; Skoumal et al., 2019). This is true even when looking at smaller sub-regions of an area experiencing induced seismicity (Figure 1). Classical Andersonian faulting theory defines the strength of a fault as

related to its orientation relative to the regional maximum principal stress direction. The theory assumes that optimal faults are uniformly stressed at failure just prior to an earthquake, with a ratio of shear to normal stress τ/σ_n equal to the static friction coefficient μ_f everywhere along the fault. These simple assumptions require an active fault to be weak (i.e., have a low value for μ_f) if its orientation differs from the optimal orientation in the present-day stress field. However, this neglects the reality that faults are geometrically complex, and may experience stress deviations that would allow limited areas of the fault to reach failure locally, at which point dynamic weakening mechanisms may occur that would allow rupture to continue outside the highly-stressed region (e.g., Dunham et al., 2011; Dempsey and Suckale, 2016; Lambert et al., 2021). Fault geometry follows a power-law distribution, and studies have suggested that faults are likely to be fractal or near-fractal over a large range of wavelengths (e.g., Dunham et al., 2011; Candela et al., 2012; Shi and Day, 2013). Such geometrical complexity should impact the along-strike distribution of pre-stress on faults as well as rupture behavior.

Given this situation, determining the distribution of prestress on faults becomes critical for understanding earthquake behavior. Although a number of studies

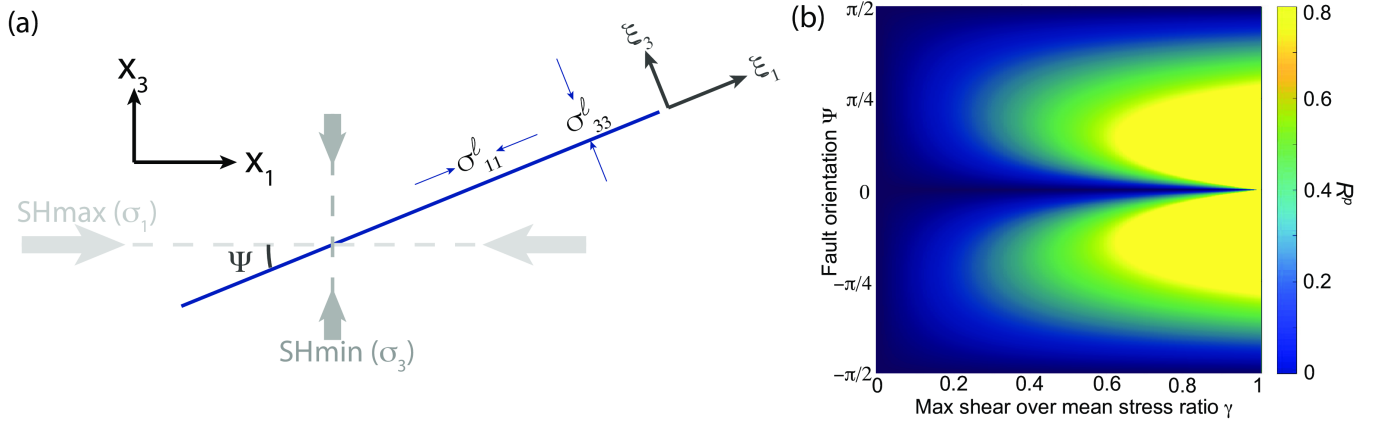


Figure 2 (a) 2D Geometry used for this study. The global coordinate system is parallel to the principal stress directions, and the fault is at angle Ψ to SHmax. (b) Resolved stress ratio on a flat fault (R^P) as a function of γ and Ψ .

have investigated the geometric roughness of faults and the impact on seismicity and ruptures (e.g., Day, 1982; Duan and Oglesby, 2007; Candela et al., 2012; Fang and Dunham, 2013; Brodsky et al., 2016; Bruhat et al., 2016; Goebel et al., 2017; Thom et al., 2017; Zielke et al., 2017; Tal et al., 2018; Kirkpatrick et al., 2020; Cattania and Segall, 2021, and many others), no studies to date of which I am aware have considered the statistical properties of pre-stress that arises from realistic geometric roughness. Development of the characteristics and distribution of stress may allow for comparison to observations and provide constraints on *in situ* stress. In this paper, I develop expressions for the statistical distribution of stress by 1) assuming a statistical distribution for fault roughness, that of a fractal geometry, 2) resolving a uniform pre-stress background field onto such fractal faults, and then 3) propagating an approximate form of the stress ratio through the transformation from the distribution for fault geometry to that for the stress ratio. This analysis assumes no slip occurring on the fault (i.e., does not account for stress changes due to slip). Doing this allows me to derive the probability distribution function (PDF) of resolved shear-over-normal stress on the fault prior to slip, which can be compared to those used in previous studies. I develop a formulation for the change in stress ratio given a change in pore pressure. Finally, I discuss some of the implications for earthquake ruptures and conclude with potential ways that the results could potentially be used to further constrain stress in the Earth's crust.

2 Analytic derivation of prestress on rough faults

2.1 Resolving a uniform remote stress field onto

Consider a 1-D flat fault embedded in a 2-D medium (Figure 2a) with a uniform background stress field (horizontal dashed line in Figure 3a). Define the global coordinate system parallel to the principal stress directions in 2-D; i.e. the x-axis is parallel to SHmax direction and the y-axis parallel to the SHmin direction. The orientation of the fault with respect to SHmax is given by

Ψ . Note that under this convention, Ψ varies between $\pm\pi/2$. In terms of the angle θ traditionally used with Mohr circles, Ψ and θ are related by $2\theta = \pi - 2\Psi$.

In the global coordinate system with a uniform background stress field, the 2-D stress tensor σ_{ij} can be written directly using the principal stresses σ_1 and σ_3 :

$$\begin{aligned} \sigma_{ij}(\mathbf{x}) &= \sigma_{ij} \\ &= \begin{bmatrix} \sigma_1 & 0 \\ 0 & \sigma_3 \end{bmatrix} \end{aligned} \quad (1)$$

SHmax is equivalent to σ_1 and Shmin to σ_3 . Parameterizing this expression in terms of the mean stress $\bar{\sigma}_m = (\sigma_1 + \sigma_3)/2$ and maximum shear stress $\tau^{\max} = (\sigma_1 - \sigma_3)/2$ (Figure 3b) gives:

$$\bar{\sigma}_{ij}^{\text{rem}} = \bar{\sigma}_m \mathbf{I} + \tau^{\max} \begin{bmatrix} 1 & 0 \\ 0 & -1 \end{bmatrix} \quad (2)$$

where \mathbf{I} is the identity matrix. To put the stress tensor into the local coordinate system (i.e., relative to the fault), rotate by Ψ using the rotation matrix \mathbf{Q} :

$$\mathbf{Q} = \begin{bmatrix} \cos \Psi & \sin \Psi \\ -\sin \Psi & \cos \Psi \end{bmatrix}. \quad (3)$$

Applying the coordinate rotation to Equation 2 gives:

$$\begin{aligned} \bar{\sigma}_{ij}^{\text{local}} &= \bar{\sigma}_m \mathbf{Q} \mathbf{Q}^T + \tau^{\max} \mathbf{Q} \begin{bmatrix} 1 & 0 \\ 0 & -1 \end{bmatrix} \mathbf{Q}^T \\ &= \bar{\sigma}_m \mathbf{I} + \tau^{\max} \begin{bmatrix} \cos(2\Psi) & -\sin(2\Psi) \\ -\sin(2\Psi) & -\cos(2\Psi) \end{bmatrix} \end{aligned} \quad (4)$$

This gives the three components of the local stress tensor as:

$$\begin{aligned} \sigma_{11}^{\text{local}} &= \bar{\sigma}_m + \cos(2\Psi)\tau^{\max} \\ \sigma_{33}^{\text{local}} &= \bar{\sigma}_m - \cos(2\Psi)\tau^{\max} \\ \sigma_{13}^{\text{local}} &= \sin(2\Psi)\tau^{\max} \end{aligned} \quad (5)$$

where the convention is that $\sigma_{11}^{\text{local}}$ is parallel to the fault, and $\sigma_{33}^{\text{local}}$ is stress normal to the (flat) fault. Shear stress $\sigma_{13}^{\text{local}} = \text{sgn}(\Psi) \sin(2\Psi)\tau^{\max}$ (taking the convention that right-lateral slip is positive), where sgn is the sign operator and $\text{sgn}(0) = 1$. The local stress state is

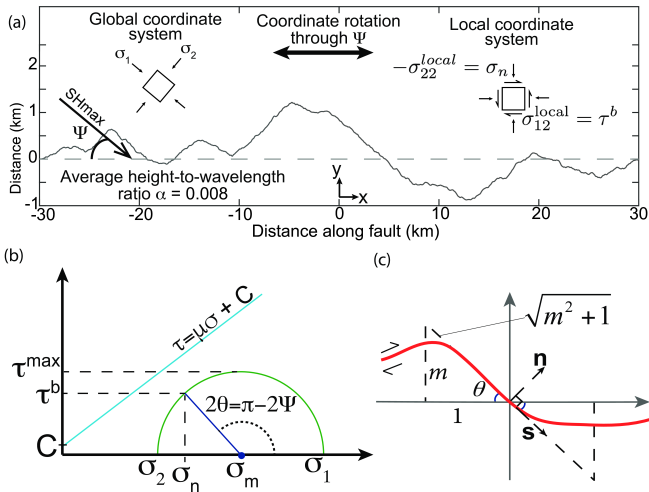


Figure 3 Geometry for resolving stress onto rough faults. (a) Global and local coordinate systems relative to a particular fault are related through an angle Ψ , the angle between the corresponding flat fault and SHmax. σ_1 and σ_2 are the maximum and minimum principal stresses in 2-D, τ^b and σ_n are the resolved shear and normal stresses on the flat fault of orientation Ψ relative to SHmax (σ_1). (b) Mohr circle diagram illustrating the various stress-related quantities and their relation to each other. C is cohesion, μ_f is friction coefficient, $\bar{\sigma}_m$ is the mean stress, and τ^{\max} is the peak shear stress. (c) Cartoon illustrating the relation between the unit normal \mathbf{n} , unit slip direction \mathbf{s} , local fault slope m , and the local angle of deviation θ^l .

written in terms of τ^{\max} , the maximum possible shear stress for a given crustal stress state, and the mean stress $\bar{\sigma}_m$. The local shear stress vanishes on faults parallel or perpendicular to the direction of SHmax (i.e. $\Psi = 0$ or ± 90 degrees, and is maximum for $\Psi = \pm 45^\circ$, as expected.

2.2 Shear-over-normal stress ratio on 2D planar faults

Resolved shear and normal stresses are given in terms of the local unit slip vector s_i and the local unit normal n_i (Jaeger et al., 2007):

$$\begin{aligned}\sigma_n &= n_i \sigma_{ij} n_j = n_1^2 \sigma_{11} + n_2^2 \sigma_{22} + 2n_1 n_2 \sigma_{12} \\ \tau &= s_i \sigma_{ij} n_j = s_1 n_1 \sigma_{11} + s_2 n_2 \sigma_{22} \\ &\quad + (n_1 s_2 + s_1 n_2) \sigma_{12}\end{aligned}\quad (6)$$

in the local coordinate system (Figure 3). In this coordinate system, the fault is parallel to the (local) x_1 axis, so $s_i = [\text{sgn}(\Psi), 0]$, and $n_i = [0, 1]$. The resolved shear stress is, as noted above, $\text{sgn}(\Psi) \sin(2\Psi) \tau^{\max}$, and resolved normal stress is $\bar{\sigma}_m - \cos(2\Psi) \tau^{\max}$. Then the shear-over-normal stress ratio on a flat fault (R^p) is

$$R^p(\Psi, \gamma) = \text{sgn}(\Psi) \frac{\sin(2\Psi)}{\gamma^{-1} - \cos(2\Psi)} \quad (7)$$

where $\gamma = \tau^{\max} / \bar{\sigma}_m$ is the ratio of the maximum shear to mean stress. Figure 2b shows the resolved stress ratio as a function of γ and Ψ . In the special case that that $\Psi = \pm \pi/4$ (i.e., 45° from SHmax), $R^p = \gamma$, as expected.

Taking the derivative of Equation 7 with respect to Ψ and setting it equal to zero gives the optimal orientation Ψ^{opt} as a function of γ :

$$\Psi^{\text{opt}} = \pm \frac{1}{2} \cos^{-1} \gamma = \pm \frac{1}{2} \cos^{-1} \frac{\tau^{\max}}{\bar{\sigma}_m} \quad (8)$$

In comparison to this analysis involving the ratio of the mean stress and maximum shear stress, traditional Mohr-Coulomb theory (Jaeger et al., 2007) states that failure will occur at the point where the Mohr circle with origin $\bar{\sigma}_m$ and radius τ^{\max} is just tangent to the friction line with slope equal to the friction coefficient μ_f and y-intercept equal to cohesion C , which is often assumed to be zero for a pre-existing plane of weakness. This is equivalent to (assuming $C = 0$ and friction angle $\phi = \pi/2 - 2\Psi$):

$$\begin{aligned}\tau^{\max} &= \bar{\sigma}_m \sin(\pi/2 - 2\Psi) \\ \rightarrow \Psi_{\text{opt}} &= \frac{1}{2} [\pi/2 - \sin^{-1} \gamma] \\ \rightarrow \Psi_{\text{opt}} &= \frac{1}{2} \cos^{-1} \gamma\end{aligned}\quad (9)$$

and plugging in $\phi = \arctan \mu_f$ shows that $\tau^{\max} / \bar{\sigma}_m = \mu_f / \sqrt{1 + \mu_f^2}$, consistent with standard arguments.

2.3 Resolved stress ratio on 2-D geometrically-rough faults

To determine the resolved stress on rough faults, use the relations for resolved shear and normal tractions written in terms of the local unit normal (\hat{n}) and tangential (\hat{s}) vectors:

$$\begin{aligned}\sigma_n^l(\xi) &= \hat{n}_i(\xi) \sigma_{ij} \hat{n}_j(\xi) \\ \tau^l(\xi) &= \hat{s}_i(\xi) \sigma_{ij} \hat{n}_j(\xi)\end{aligned}\quad (10)$$

where ξ is position along the fault and \hat{s} is the unit vector parallel to the fault pointing in the direction of slip (note that this analysis is for static stress so no slip occurs; slip direction refers to right- or left- lateral and is based on the orientation of SHmax). The local normal and slip vectors can be written in terms of local ‘‘slope’’ m , defined as the local orientation of a point on the fault in relation to the overall fault orientation (Figure 3c).

$$\begin{aligned}\mathbf{n} &= \begin{bmatrix} n_1 \\ n_2 \end{bmatrix} \\ &= \begin{bmatrix} -\sin(\tan^{-1}(m)) \\ \cos(\tan^{-1}(m)) \end{bmatrix} \\ &= \frac{1}{\sqrt{m^2 + 1}} \begin{bmatrix} -m \\ 1 \end{bmatrix}\end{aligned}\quad (11)$$

and

$$\begin{aligned}\mathbf{s} &= \begin{bmatrix} s_1 \\ s_2 \end{bmatrix} \\ &= \frac{\text{sgn}(\Psi)}{\sqrt{m^2 + 1}} \begin{bmatrix} 1 \\ m \end{bmatrix}.\end{aligned}\quad (12)$$

where $\mathbf{s} \cdot \mathbf{n} = 0$ due to orthogonality (see Figure 3). Local resolved normal and shear stresses are calculated by

substituting Equations 11 and 12 into Equation 10. The resolved normal stress is:

$$\sigma_n^l = \frac{\bar{\sigma}_m}{m^2 + 1} \times \left[(1 + m^2) - \cos(2\Psi)(1 - m^2)\gamma - 2m \sin(2\Psi)\gamma \right] \quad (13)$$

and the corresponding shear stress is:

$$\tau^l = \frac{\text{sgn}(\Psi)\tau^{\max}}{m^2 + 1} \times (-2m \cos(2\Psi) + \sin(2\Psi) [1 - m^2]). \quad (14)$$

Taking the ratio gives the expression for the local resolved shear over normal stress ratio R^l as a function of the overall fault orientation, the local slope, and the stress state encapsulated by γ :

$$R^l(\sigma_{ij}, \Psi, m) = \frac{\text{sgn}(\Psi) [(1 - m^2) \sin(2\Psi) - 2m \cos 2\Psi]}{(1 + m^2)\gamma^{-1} - 2m \sin(2\Psi) - (1 - m^2) \cos 2\Psi} \quad (15)$$

Note that only fault slope m varies with position on the fault ξ .

2.4 Statistical description of fault roughness

Everything to this point has been done without any assumptions made about the statistical properties of fault geometry. Now suppose that fault slope, m , follows a Normal distribution; i.e., $\varphi(m) \sim \mathcal{N}(0, \sigma_m^2)$. $\varphi(m)$ is the (Gaussian) probability distribution for m , and $R^l = g(m)$ is the resolved stress as a function of slope. This is consistent with previous work (Dunham et al., 2011) that showed fault slope is Gaussian for self-similar (fractal) faults with average amplitude-to-wavelength ratio α . Such faults are characterized by a power spectral ratio of the form

$$P(k) = (2\pi)^3 \alpha^2 |k|^{-3} \quad (16)$$

where k is wavenumber (see Discussion) (Dunham et al., 2011). For 1-D band-limited self-similar faults, m is Gaussian-distributed with zero mean and a standard deviation proportional to α (Dunham et al., 2011; Fang and Dunham, 2013):

$$\sigma_m^2 \approx 8\pi^2 \alpha^2 \ln(k_{\max}/k_{\min}) \quad (17)$$

where k_{\max} and k_{\min} are the maximum and minimum roughness wavenumbers, respectively. As an example, for faults 30 km long and minimum roughness wavelength of a few meters, $k_{\max} \approx 1$, $k_{\min} \approx 10^{-4}$, and $\sigma_m \approx 25\alpha$.

At higher roughness (larger α), two differences occur compared to the smooth fault case. First, the average stress ratio required for 5% of points to reach failure (arbitrarily assumed 0.7) is now much lower, 0.552 in Fig. 4b and 0.517 in Fig. 4c. In other words, for fixed peak stress the background or average stress level required to reach peak stress is inversely proportional to the roughness level. Second, much of the fault is also further away from failure than the background. These effects do depend on the minimum and maximum wavelength, but likely would be more pronounced

for natural faults, as roughness extends down to nucleation wavelengths (Dunham et al., 2011; Fang and Dunham, 2013; Heimisson, 2020). The fact that fault slope is normally distributed can be exploited to determine the statistical distribution of fault stress using Equation 15. To do this, we note that for a random variable m with probability density function $\Psi(m)$, and a monotonic and one-to-one transformation $R^l = g(m)$ between m and R^l , the inverse transformation $g^{-1}(R^l)$ can be used to derive the distribution of the random variable R^l , $\varphi(R^l)$. The general expression is:

$$\varphi(R^l) = \Psi(g^{-1}(R^l)) \left| \frac{dg^{-1}(R^l)}{dR^l} \right| \quad (18)$$

Substituting a Gaussian distribution with variance σ_m^2 for $\Psi(m)$ gives:

$$\varphi(R^l) = \mathcal{N}(g^{-1}(R^l), \sigma_m^2) \left| \frac{dg^{-1}(R^l)}{dR^l} \right| \quad (19)$$

Approximations of various orders can be derived using a polynomial expansion of Equation 15:

$$\begin{aligned} & \frac{(1 - m^2) \sin(2\Psi) - 2m \cos 2\Psi}{(1 + m^2)\gamma^{-1} - 2m \sin(2\Psi) - (1 - m^2) \cos 2\Psi} \\ &= \frac{\sin(2\Psi) - 2 \cos 2\Psi m - \sin(2\Psi)m^2}{(\gamma^{-1} - \cos 2\Psi) - 2 \sin(2\Psi)m + (\gamma^{-1} + \cos 2\Psi)m^2} \\ &= \frac{A - 2Bm - Am^2}{C - 2Am + Dm^2} = \sum_{k=0}^{\infty} a_k m^k \end{aligned} \quad (20)$$

which, after multiplying through by the denominator and expanding out and collecting terms proportional to powers of m , gives:

$$\begin{aligned} A - 2Bm - Am^2 &= a_0 C + (-2a_0 A + a_1 C)m \\ &+ \sum_{k=2}^{\infty} (a_{k-2} D - 2a_{k-1} A + a_k C)m^k \end{aligned} \quad (21)$$

for $A = \sin 2\Psi$, $B = \cos 2\Psi$, $C = \gamma^{-1} - \cos 2\Psi$, and $D = \gamma^{-1} + \cos 2\Psi$, and coefficients a_k to be determined. Eq. 21 can be recursively solved for as many coefficient terms as desired. Keeping only first order terms and substituting the result back into Equation 15 gives the first-order expression for the resolved stress on faults:

$$\begin{aligned} R^l &\approx \text{sgn}(\Psi) [a_0 + a_1 m] \\ &= \text{sgn}(\Psi) \left[\frac{\sin 2\Psi}{\gamma^{-1} - \cos 2\Psi} + \frac{2}{\gamma} \frac{\gamma - \cos 2\Psi}{(\gamma^{-1} - \cos 2\Psi)^2} m \right] \end{aligned} \quad (22)$$

Note that a_0 is simply the planar fault value, and also the mean of the distribution (because m has a zero mean). Note that Ψ and γ are not independent; they are related through the local stress tensor. Therefore, not all possible combinations of Ψ and γ are valid for consistent stress tensors.

The next step is to invert Equation 22 for m , calculate the absolute derivative with respect to R^l , and substitute the inverse transformation into the distribution of m . Inverting Eq. 22 gives:

$$\begin{aligned} m &= \frac{\gamma \text{sgn}(\Psi) (\gamma^{-1} - \cos 2\Psi)^2}{2 (\gamma - \cos 2\Psi)} \times \\ &\left[R^l - \frac{\sin 2\Psi \text{sgn}(\Psi)}{(\gamma^{-1} - \cos 2\Psi)} \right] \end{aligned} \quad (23)$$

and the derivative term is:

$$\begin{aligned} \left| \frac{dg^{-1}(R^l)}{dR^l} \right| &= \left| -\frac{\gamma (\gamma^{-1} - \cos 2\Psi)^2}{2 (\gamma - \cos 2\Psi)} \right| \\ &= \frac{\gamma (\gamma^{-1} - \cos 2\Psi)^2}{2 |\gamma - \cos 2\Psi|} \end{aligned} \quad (24)$$

and so (noting that m has zero mean)

$$\begin{aligned} \varphi(R^l) &= \frac{1}{\sqrt{2\pi\sigma_{R^l}^2}} e^{-\frac{1}{2\sigma_{R^l}^2} ([R^l - \mu_{R^l}])^2} \\ &= \mathcal{N}(\mu_{R^l}, \sigma_{R^l}^2) \end{aligned} \quad (25)$$

where the mean is

$$\mu_{R^l} = \text{sgn}(\Psi) \frac{\sin 2\Psi}{\gamma^{-1} - \cos 2\Psi} \quad (26)$$

and the standard deviation is proportional to σ_m :

$$\sigma_{R^l} = \frac{(1 - \gamma \cos 2\Psi)^2}{2\gamma|\gamma - \cos 2\Psi|} \sigma_m. \quad (27)$$

Thus, to first order, stress on a rough fault is Gaussian, with a mean equal to the stress on a planar fault of the same orientation and deviations proportional to α . Also note that, as $\gamma \rightarrow 1$ (i.e. larger differential stress), $\sigma_{R^l} \rightarrow 0$, and if $\gamma \rightarrow 0$ (more uniform stress state), σ_{R^l} becomes large.

Although the derivation so far is helpful for a basic understanding, it is limited because the first-order approximation breaks down if the fault is close to optimally-oriented. Keeping the second-order term:

$$a_2 = \frac{2 \sin 2\Psi}{\gamma} \frac{2\gamma - \cos 2\Psi - \gamma^{-1}}{(\gamma^{-1} - \cos 2\Psi)^3} \quad (28)$$

provides a more accurate but non-Gaussian approximation of the distribution of on the resolved stress ratio R^l . Keeping three terms and then transforming as above requires solving a quadratic equation for m :

$$\begin{aligned} R^l &= \text{sgn}(\Psi) (a_0 + a_1 m + a_2 m^2) \\ \rightarrow 0 &= a_2 m^2 + a_1 m + (a_0 - R^l \text{sgn}(\Psi)) \\ \rightarrow m &= \frac{-a_1 \pm \sqrt{a_1^2 - 4(a_0 - R^l \text{sgn}(\Psi)) a_2}}{2a_2} \\ &= \frac{-a_1 \pm \Gamma}{2a_2} \end{aligned} \quad (29)$$

where Γ^2 is the term inside the square root: $a_1^2 - 4(a_0 - R^l \text{sgn}(\Psi)) a_2$. The gradient is also needed:

$$\frac{dg^{-1}}{dR^l} = \frac{1}{\Gamma} \quad (30)$$

Then, plugging the above expressions into the Normal distribution gives:

$$\varphi(R^l) = \frac{1}{\sqrt{2\pi\sigma_m^2}} \frac{1}{\Gamma} e^{-\frac{1}{2\sigma_m^2} \left(\frac{\Gamma - a_1}{2a_2}\right)^2} \quad (31)$$

where the positive solution in the quadratic is the correct one.

3 Results

Figure 4 shows three plots with the same fault orientation (Ψ) and geometry and three different values of α : .001, 0.005, and 0.01. I.e., scaling these faults to the same roughness level would result in identical fault geometry. For these three examples, R^p is chosen differently for each case such that approximately 5% of points on the fault have $R^l \geq 0.7$. This represents in each case a scenario where some points are just at failure, assuming a friction coefficient of 0.7. Note that the fault profiles are shown in the lower-right corner of each subplot at true (i.e., non-exaggerated) scale. The faults are band-limited with a minimum roughness wavelength of 30 m and the resolved stress ratio calculated for each.

Resolved stress in Fig. 4 varies by about 15% of R^p for $\alpha = 0.001$, ranging from approximately 0.6 to 0.7. For $\alpha = 0.005$, variability is about 82% of R^p (0.35-0.8), and for $\alpha = 0.01$ is about 116% of R^p (0.1 - 0.7). As roughness level increases, the mean stress value required to have 5% of points at the failure level (assumed 0.7) decreases. At the highest roughness level, the peak stress ratio can be seen to be about 0.7, while at lower roughness levels and higher values of R^p , resolved stress does not reach the peak ratio value, showing that the fault is further from optimal orientation. This occurs because keeping the orientation of SHmax fixed and changing τ^b/σ_m requires that the absolute stress magnitudes change. The result is that a rougher fault having a peak stress ratio at failure is, on average, farther from failure than a smoother fault also having peak stress at failure. Since the geometry of each of the faults is the same and only the roughness level varies, the stress profiles are also similar, with the exception of the truncated values at the peak stress ratio for case (c).

Fig. 5a shows the power spectral densities (PSDs) of fault geometry, fault slope, and resolved fault stress, while Fig. 5b shows the PSDs of stress ratio for each of the fault cases shown in Fig. 4. The PSD for a fractal (i.e., self-similar) fault profile such as I have adopted here will have a spectrum proportional to $|k|^{-3}$. The slope is the first spatial derivative of the profile and will thus have a spectrum proportional to $|k|^{-1}$. From Equation 15, resolved static stress is a polynomial function of slope m , and so can be written as a linear combination of powers of m . This implies that the spectrum is also a linear function of the transform variable \hat{m} and has the same slope (Dunham et al., 2011) (Fig. 5a). The difference between faults of different roughness manifests as a vertical offset on the PSD plot (Fig. 5b).

Figure 6 compares numerically-simulated and analytical probability distributions (utilizing the second-order approximate solution) of resolved stress ratio. For each subplot, parameters that are not the focus of the plot are kept constant, with $\Psi = 50^\circ$, $R^p = 0.5$, and $\alpha = 0.01$. The numerical distributions in each plot are normalized to unit area to represent probabilities; the analytical solutions are normalized by definition. Distributions vary in shape depending on how close the mean stress ratio is to the peak stress ratio (i.e., the value of the stress ratio at the optimal fault orientation) and how spread the distribution is. Distributions where all points

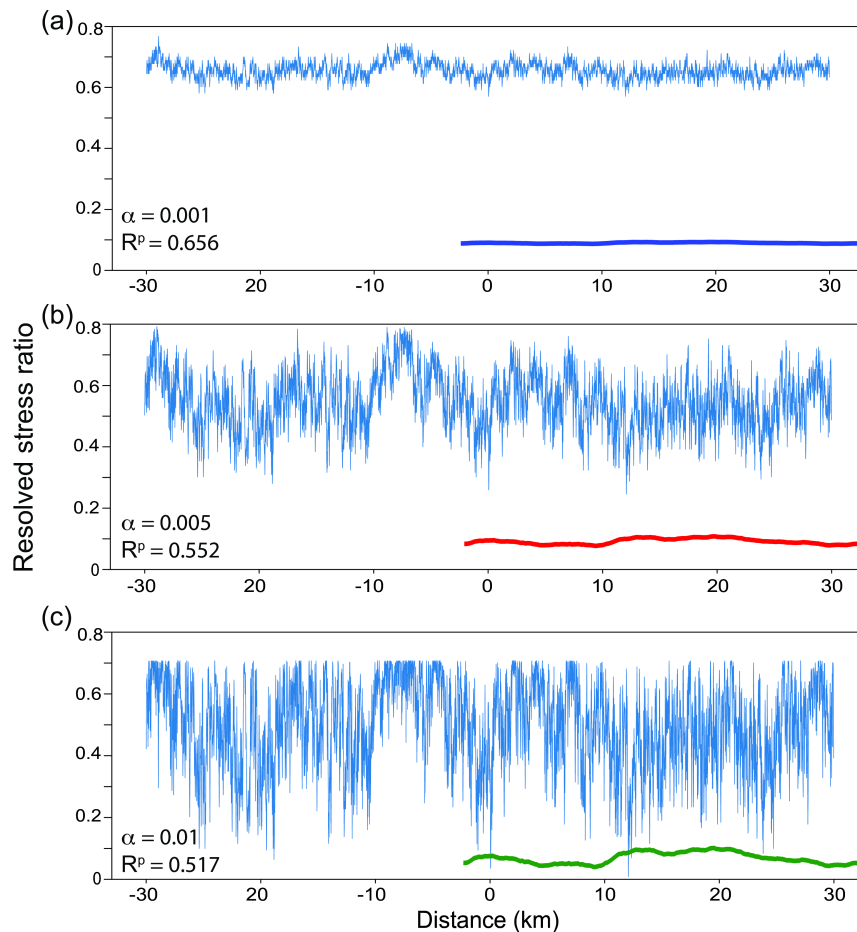


Figure 4 Resolved shear/normal stress ratio for the same fault profile at three different roughness values (profiles shown in the lower-right corners) using Equation 15. The fault in each case is 30 km long, with a minimum roughness wavelength of 30 m, oriented at $\Psi = 50^\circ$. Note that the fault profiles are at true scale relative to each other but not on the same scale as the stress profiles. In each panel the background stress tensor is chosen such that 5% of points have $R^l \geq 0.7$. γ is the flat-fault stress ratio and also the mean stress on each fault.

have ratios far from the peak value are approximately Gaussian, while distributions where the mean is close to the peak appear exponential decaying to lower values. Distributions intermediate to these end-members are approximately Gaussian away from the peak, but are truncated with extra probability at the peak. The latter cases are where the second-order approximation derived above breaks down the most.

Fig. 6a shows how stress changes while increasing the planar-fault static stress ratio R^p from 0.2 to 0.6. The main point to note here is that both the shape and the spread of the distribution changes, and in particular the peak stress ratio ($\max R^l$) increases faster than the mean of the distribution (which equals R^p). (Note that I have not truncated the distributions at the friction value.) Static stress on a rough fault may locally be well above the value expected based on the overall orientation with respect to the stress orientation. Assuming that a planar fault at optimal orientation with friction equal to 0.6 would fail in the prevailing stress regime, a fault non-optimally oriented with a background stress ratio of only 0.5 has some segments at failure.

Fig. 6b shows how the distributions change with the orientation of the fault with respect to the maximum principal stress, Ψ . Of particular note is that faults

that are well away from optimally orientated have a very broad range of resolved stresses, with some points on the fault likely exceeding fault friction, while some points have nearly zero resolved shear stress. At the other extreme, faults with optimal orientation are almost entirely at or very close to the peak stress ratio.

Fig. 6c shows how the distributions vary with fault roughness level. As expected, increasing roughness leads to increasing variance in the resolved stress ratio. At low roughness, and for faults not optimally-oriented, the stress ratio is Gaussian with a mean at the planar fault value. At higher roughness, some points on the fault become optimally oriented, leading to truncation of the distribution, and at the highest roughness the distribution is clearly non-Gaussian. The distribution for $\alpha = 0.01$ is skewed right and long-tailed to the left, resulting in much more complex fault stress, as can be seen by comparing back to Fig. 4c.

The difference between the analytical approximation (Eq. 31) and the numerically-simulated results is generally quite small. The exceptions are for those cases where the shape of the stress ratio distribution is intermediate between the two end-member distributions: a shape close to Gaussian and a shape close to a reverse exponential distribution. As noted above, this occurs as

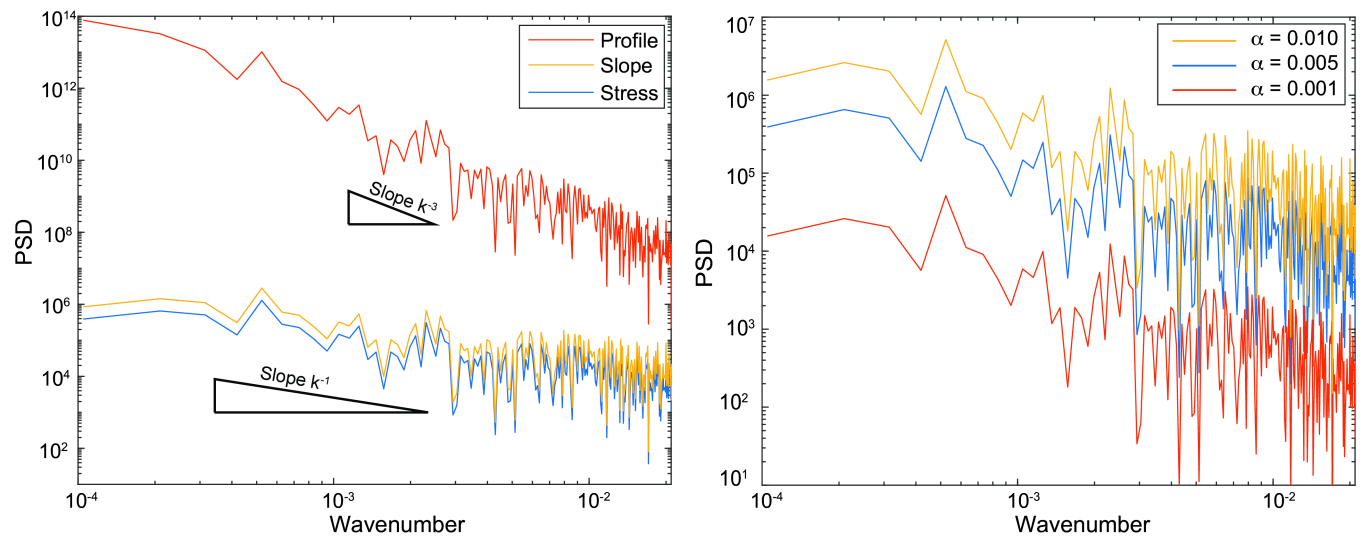


Figure 5 (a) Comparing PSDs for fault profile $h(x)$, fault slope $m(x)$, and resolved shear-to-normal stress ratio $R^m(x)$, assuming a minimum roughness wavelength of 300 m and total fault length of 60 km. $\alpha = 0.005$ here. (b) Comparing PSDs of resolved stress ratio for three different levels of roughness. In both plots, the x-axis limits are k_{\min} and k_{\max} .

the mean stress ratio approaches the peak stress ratio but is still below it. Examples of this include Fig. 6a, $R^p = 0.4$ and .5, Fig. 6b, $\Psi = 50$, and Fig. 6c, $\alpha = 0.01$. In these cases, the second-order approximation starts to break down and the approximate solution becomes less accurate.

4 Discussion

4.1 Reaching frictional failure on geometrically-rough faults

From the results presented here, one first-order effect of geometric roughness is to reduce the stress required to achieve the failure stress ratio at some locations on the fault. A planar fault obviously has only one value for the shear over normal stress ratio along the entire length of the fault, and many studies that consider fault stress take this as a starting assumption, including Andersonian faulting theory. A geometrically rough fault, however, may have significant portions of the fault that are well away from failure (for a fault near optimal orientation) that could pin the well-oriented segments of the fault until it reaches the failure threshold; this has previously been proposed for fault networks with faults of various orientations (Fletcher et al., 2016). The concept of a keystone fault may thus extend not only to fault networks but also to a single rough fault. The converse point is that some fault segments may be well-oriented for failure even on an overall misoriented fault: in Fig. 4, the background stress ratio required on a moderately rough fault for 5% of points to reach a failure threshold is only 79% of that required for the corresponding planar fault (i.e., a fault having the exact same overall mean stress ratio), and only 74% for the very rough fault (Fig. 4). Another possibility is that fault segments with lower resolved stress due to geometry may rupture as small earthquakes in the well-orientated segments, until stress builds up enough on the misoriented segments to allow rupture to propagate through

the entire fault. Such a scenario would imply that segment boundaries may be persistent for multiple earthquake cycles, but then break in large penultimate earthquakes. All of these issues are tied to the overall roughness level, implying that the overall behavior of a fault may be closely related to its degree of roughness.

4.2 Characteristics of geometric rough stress

Andrews (1980) found using two different approaches that stress on faults should have a $1/k$ spectrum. The first assumes that earthquakes are self-similar and that stress changes during rupture reflect spatial fluctuations in the initial stress field stemming from slip in past earthquakes. Mean square stress decays as $|k|^{-2\delta-1}$, where earthquakes with radius a produce stress drops a^δ . Assuming that stress drop is independent of size results in a power spectral density (PSD) proportional to $|k|^{-1}$. The second argument is based on an approximate stochastic model of fault energetics, wherein slip during an earthquake is the sum of a smooth long-wavelength coherent part and a shorter-wavelength (shorter than rupture size $\propto a$) random part which is assumed self-similar between the wavelength of the event size (a) and grain size. Adding the smooth and coherent slip, the resulting stress change also has coherent and stochastic components. Summing the contributions from all past events results in a spectrum proportional to k^{-1} if stress drop is independent of size. Experimental measurements of fault geometry over many orders of magnitude suggest that roughness on faults in the crust are close to self-similar (e.g., Sagy and Brodsky, 2009; Candela et al., 2009, 2012; Shi and Day, 2013; Fang and Dunham, 2013; Thom et al., 2017; Kirkpatrick et al., 2020). In this study, we assume fractal fault geometry, and Fig. 5 shows that power spectrum of the resolved stress ratio obeys the $1/k$ rule.

In contrast to some previous studies (e.g., Dieterich et al., 2015; Dempsey and Suckale, 2016; Kroll and Cochran, 2021), resolved stress due to geometric rough-

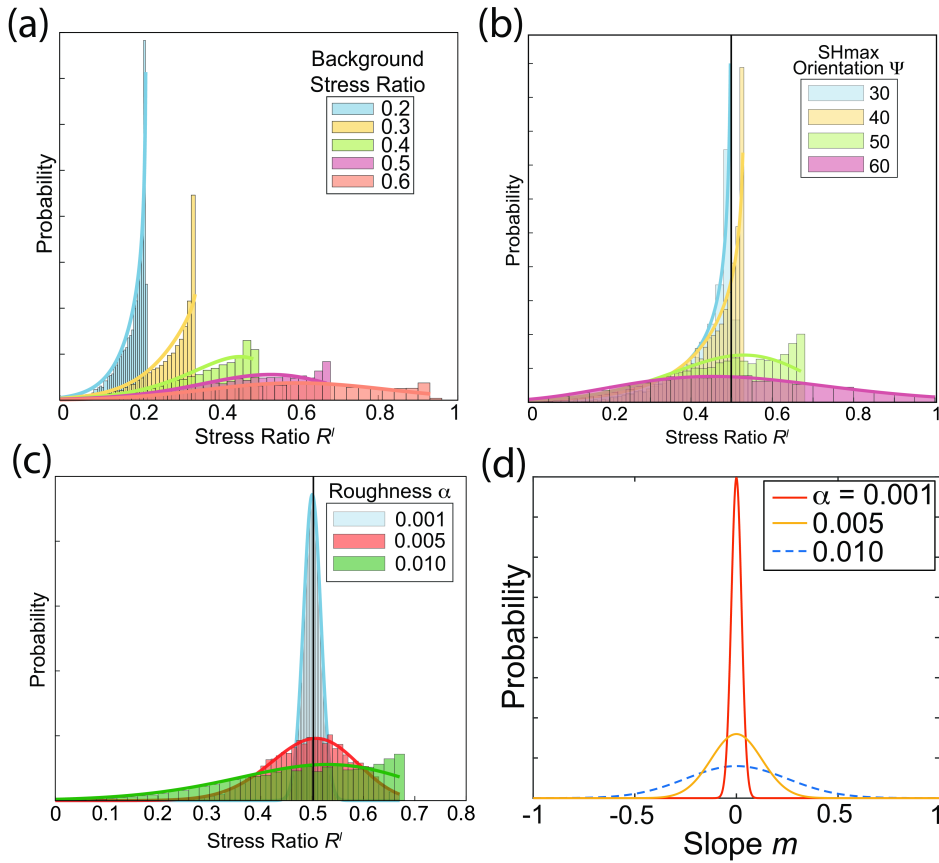


Figure 6 Comparison between numerical and analytical distributions of resolved shear-to-normal stress ratio for the second-order approximation. Parameter values unless specified in the plot are $R^p = 0.5$, $\Psi = 50^\circ$, and $\alpha = 0.01$. The black vertical line in (b) and (c) denotes the background stress ratio R^p . (a) Increasing the background stress R^p . The change in the shape of the distribution reflects the fact that the maximum possible stress ratio and the highest resolved stress ratio both increase faster than the background. (b) Changing the orientation of SHmax. At this particular value of the background stress, orientations closest to optimal have the lowest variance. (c) Changing α . Faults with larger roughness have larger deviations in slope, which translates to larger deviations in resolved friction. (d) PDFs on fault slope for several values of α , using a Gaussian distribution with $\sigma_m \approx 25\alpha$. Slopes in the roughest case can be rather large; slopes slightly above 1 are possible.

ness does not have long upper tails. While this may seem intuitive (stress is maximum at the optimal orientation), studies of heterogeneous fault stress sometimes adopt distributions with upper tails (Dieterich et al., 2015; Dempsey and Suckale, 2016). Upper tails can only occur if external sources of stress act on a fault that is far from failure; e.g. perturbations from nearby slip or local pore pressure increase. Note that “far from failure” will depend somewhat on fault roughness level. The fault must be far from failure or presumably an increase in stress would immediately trigger an earthquake to occur. For stress changes, e.g. from pore pressure, that act over the length scale of the entire fault, an expression for the rate of change of resolved stress can be derived by differentiating Eq. 15 with respect to the perturbation. The resolved effective stress ratio given a change in pore-pressure (only accounting for the impact on effective normal stress) is

$$R^l(\sigma_{ij}, \Psi, m, \Delta P) = \frac{\text{sgn}(\Psi) [(1 - m^2) \sin(2\Psi) - 2m \cos 2\Psi]}{(1 + m^2)\bar{\gamma}^{-1} - 2m \sin(2\Psi) - (1 - m^2) \cos 2\Psi} \quad (32)$$

where $\bar{\gamma} = \tau^{\max}/(\bar{\sigma}_m - \Delta P)$. Taking the partial deriva-

tive of Eq. 32 with respect to ΔP gives the rate of change in the resolved stress ratio (again assuming that the pore pressure change acts uniformly over the entire fault):

$$\frac{\partial R^l}{\partial \Delta P} = \frac{R^l}{\tau^{\max}} \times \frac{-(1 + m^2)}{[(1 + m^2)\bar{\gamma}^{-1} - 2m \sin(2\Psi) - (1 - m^2) \cos 2\Psi]} \quad (33)$$

Equation 33 implies that perturbations to the normal stress result in stress ratio changes that (1) impact optimally-oriented fault segments more than non-optimal segments (i.e. are proportional to the stress ratio R^l), and (2) are inversely proportional to the peak shear stress. Note that even though R^l does not depend on the absolute background stress state, the rate of change in the local ratio does depend on the absolute stress (τ^{\max} in Eq. 33). Such a situation creates potential for future studies to consider whether controlled changes in pore pressure could be used to probe the state of stress on crustal faults by monitoring the rate of earthquakes and the pore pressure change.

4.3 Fault roughness and earthquakes

Stress heterogeneity arising from geometric roughness is known to play an important role in how earthquakes start and stop (Fang and Dunham, 2013; Dieterich et al., 2015; Tal et al., 2018). Spatial variability in the resolved stress ratio impact ruptures in dynamic simulations (Fang and Dunham, 2013; Maurer et al., 2020; Bruhat et al., 2016; Cattania and Segall, 2021; Kroll and Cochran, 2021). This effect is consistent with the observation of the large stress changes that result from fault bends, even slight ones (Figure 4), and suggests that dynamic characteristics of earthquakes, including size and rupture speed, may be influenced or even controlled by fault roughness (e.g., Fang and Dunham, 2013). Considering Figure 4, it seems likely that the nature and size distribution of earthquakes on the three faults would likely be very different. Since fault geometry is easier to constrain than *in situ* fault stress, systematic study of fault geometry across scales and how earthquakes correspond to various roughness levels on natural faults could provide valuable insight into future earthquake characteristics of a given fault. The results presented here provide analytic expressions for stress distributions that could be incorporated into studies on fault stress and slip, particularly in laboratory settings where background loading is well known.

5 Conclusions

I provide analytic solutions for stress on rough faults under 2D conditions, under which there are only three parameters to consider for a given fault: fault orientation relative to SHmax, background or average stress ratio, and roughness level. From these, and assuming that fault slope is Gaussian distributed, which is true for self-similar faults, I derive the statistical distribution of the stress ratio on rough faults. Stress variations due to fault roughness has the following characteristics:

1. The mean stress is always equal to the planar-fault value.
2. To first order, the distribution of stress is approximately Gaussian with a standard deviation proportional to fault roughness level α .
3. To second order, the stress distribution truncates at the optimal orientation and is skewed to lower values, rather than having long upper tails.

The distribution varies between two end-member distributions, Gaussian and reverse exponential (i.e., exponential decrease to lower values). A simple criteria for the two end-members is using the first-order approximation for the stress distribution; when the peak stress ratio is more than two standard deviations from the mean stress ratio, the distribution is approximately Gaussian, and when the mean stress ratio is approximately equal to the peak stress, the distribution is reverse exponential. Intermediate to these two end-members are distributions that look like a truncated Gaussian, where the shape of the distribution depends on how close the mean stress is to the peak stress. The

resolved fault stress ratio does not have long upper tails. For faults near optimal orientation, the stress distribution has a reverse exponential shape, and is skewed towards lower stress values. Faults that are not optimally orientated may still have significant areas near the failure stress, and vice-versa. The implication is that for any given background stress field, there may be a range of fault orientations that have at least some segments near the failure stress, depending on the roughness level of the faults, and optimally-oriented faults may have segments well away from failure. This is consistent with the idea of a keystone fault, where a fault may be overall well-oriented for failure with respect to the background stress field, but have some segments which pin the fault in place and prevent it from slipping until the stress reaches a high enough level to allow ruptures to propagate through those misoriented segments. The distribution of stress on rough faults is likely to have strong impacts on seismicity, and could potentially be used to probe the absolute stress level under certain conditions. Future work should investigate these possibilities and utilize more realistic stress distributions in order to better simulate rupture dynamics and investigate crustal seismicity.

Acknowledgements

The author thanks P. Segall, E. Dunham, C. Cattania, and M. Kerr for helpful discussions on this topic, as well as constructive reviews from three anonymous reviewers that substantially improved the manuscript.

Data and code availability

No data were used in this study. Codes for replicating Figures 1b, 3, 4, and 5 as well as text files containing the fault profiles shown in Figure 3 are archived at Maurer (2022).

Competing interests

The author is not aware of any competing interest.

References

- Allam, A. A., Kroll, K. A., Milliner, C. W. D., and Richards-Dinger, K. B. Effects of Fault Roughness on Coseismic Slip and Earthquake Locations. *Journal of Geophysical Research: Solid Earth*, 124(11):11336–11349, nov 2019. doi: <https://doi.org/10.1029/2018JB016216>.
- Ando, R. and Kaneko, Y. Dynamic Rupture Simulation Reproduces Spontaneous Multifault Rupture and Arrest During the 2016 Mw 7.9 Kaikoura Earthquake. *Geophysical Research Letters*, 45(23):12, 812–875, 883, dec 2018. doi: <https://doi.org/10.1029/2018GL080550>.
- Andrews, D. J. A stochastic fault model: 1. Static case. *Journal of Geophysical Research: Solid Earth*, 85:3867–3877, 1980. doi: [10.1029/JB085iB07p03867](https://doi.org/10.1029/JB085iB07p03867).
- Bhat, H. S., Dmowska, R., Rice, J. R., and Kame, N. Dynamic Slip Transfer from the Denali to Totschunda Faults, Alaska:

- Testing Theory for Fault Branching. *Bulletin of the Seismological Society of America*, 94(6B):S202–S213, dec 2004. doi: 10.1785/0120040601.
- Brodsky, E. E., Kirkpatrick, J. D., and Candela, T. Constraints from fault roughness on the scale-dependent strength of rocks. *Geology*, 2016. doi: 10.1130/G37206.1.
- Bruhat, L., Fang, Z., and Dunham, E. M. Rupture complexity and the supershear transition on rough faults. *Journal of Geophysical Research: Solid Earth*, 121:210–224, 1 2016. doi: 10.1002/2015JB012512.
- Candela, T., Renard, F., Bouchon, M., Brouste, A., Marsan, D., Schmittbuhl, J., and Voisin, C. Characterization of fault roughness at various scales: Implications of three-dimensional high resolution topography measurements. *Pure and Applied Geophysics*, 166:1817–1851, 2009. doi: 10.1007/s00024-009-0521-2.
- Candela, T., Renard, F., Klinger, Y., Mair, K., Schmittbuhl, J., and Brodsky, E. E. Roughness of fault surfaces over nine decades of length scales. *Journal of Geophysical Research: Solid Earth*, 117, 8 2012. doi: 10.1029/2011JB009041.
- Cattania, C. and Segall, P. Precursory Slow Slip and Foreshocks on Rough Faults. *Journal of Geophysical Research: Solid Earth*, 126 (4), apr 2021. doi: 10.1029/2020JB020430.
- Day, S. M. Three-dimensional simulation of spontaneous rupture: The effect of nonuniform prestress. *Bulletin of the Seismological Society of America*, 72(6A):1881–1902, dec 1982. doi: 10.1785/BSSA07206A1881.
- Dempsey, D. and Suckale, J. Collective properties of injection-induced earthquake sequences: 1. Model description and directivity bias. *Journal of Geophysical Research: Solid Earth*, 121: 3609–3637, 2016. doi: 10.1002/2015JB012550.
- Dempsey, D., Suckale, J., and Huang, Y. Collective properties of injection-induced earthquake sequences: 2. Spatiotemporal evolution and magnitude frequency distributions. *Journal of Geophysical Research: Solid Earth*, 121:3638–3665, 2016. doi: 10.1002/2015JB012551.
- Dieterich, J. H., Richards-Dinger, K. B., and Kroll, K. A. Modeling Injection-Induced Seismicity with the Physics-Based Earthquake Simulator RSQSim. *Seismological Research Letters*, 86: 1102–1109, 2015. doi: 10.1785/0220150057.
- Duan, B. and Oglesby, D. D. Nonuniform prestress from prior earthquakes and the effect on dynamics of branched fault systems. *Journal of Geophysical Research: Solid Earth*, 112(B5), 2007. doi: https://doi.org/10.1029/2006JB004443.
- Dunham, E. M., Belanger, D., Cong, L., and Kozdon, J. E. Earthquake ruptures with strongly rate-weakening friction and off-fault plasticity, part 2: Nonplanar faults. *Bulletin of the Seismological Society of America*, 101:2308–2322, 2011. doi: 10.1785/0120100076.
- Fang, Z. and Dunham, E. M. Additional shear resistance from fault roughness and stress levels on geometrically complex faults. *Journal of Geophysical Research: Solid Earth*, 118:3642–3654, 2013. doi: 10.1002/jgrb.50262.
- Fletcher, J. M., Oskin, M. E., and Teran, O. J. The role of a keystone fault in triggering the complex El Mayor-Cucapah earthquake rupture. *Nature Geosci*, 9(4):303–307, 2016. doi: 10.1038/N-GEO2660.
- Goebel, T. H. W., Kwiatak, G., Becker, T. W., Brodsky, E. E., and Dresen, G. What allows seismic events to grow big?: Insights from b-value and fault roughness analysis in laboratory stick-slip experiments. *Geology*, 45(9):815–818, jul 2017. doi: 10.1130/G39147.1.
- Heimisson, E. R. Crack to pulse transition and magnitude statistics during earthquake cycles on a self-similar rough fault. *Earth and Planetary Science Letters*, 537:116202, 2020. doi: https://doi.org/10.1016/j.epsl.2020.116202.
- Jaeger, J. C., Cook, N. G. W., and Zimmerman, R. W. *Fundamentals of rock mechanics - Fourth edition*. 2007. doi: 10.1016/0040-1951(77)90223-2.
- King, G. and Nábělek, J. Role of Fault Bends in the Initiation and Termination of Earthquake Rupture. *Science*, 228(4702): 984–987, may 1985. doi: 10.1126/science.228.4702.984.
- Kirkpatrick, J. D., Edwards, J. H., Verdecchia, A., Kluesner, J. W., Harrington, R. M., and Silver, E. A. Subduction megathrust heterogeneity characterized from 3D seismic data. *Nature Geoscience*, 13(5):369–374, may 2020. doi: 10.1038/s41561-020-0562-9.
- Kroll, K. A. and Cochran, E. S. Stress Controls Rupture Extent and Maximum Magnitude of Induced Earthquakes. *Geophysical Research Letters*, 48(11):e2020GL092148, jun 2021. doi: https://doi.org/10.1029/2020GL092148.
- Lambert, V., Lapusta, N., and Faulkner, D. Scale Dependence of Earthquake Rupture Prestress in Models With Enhanced Weakening: Implications for Event Statistics and Inferences of Fault Stress. *Journal of Geophysical Research: Solid Earth*, 126(10):e2021JB021886, oct 2021. doi: https://doi.org/10.1029/2021JB021886.
- Lund-Snee, J.-E. and Zoback, M. D. State of stress in areas of active unconventional oil and gas development in North America. *AAPG Bulletin*, 106:355–385, 2 2022. doi: 10.1306/08102120151.
- Maurer, J. Stress on Rough Faults. Sep 2022. doi: https://doi.org/10.17605/OSF.IO/Z7YF2.
- Maurer, J., Dunham, E. M., and Segall, P. Role of Fluid Injection on Earthquake Size in Dynamic Rupture Simulations on Rough Faults. *Geophysical Research Letters*, 47:e2020GL088377, 2020. doi: https://doi.org/10.1029/2020GL088377.
- Oglesby, D. D. The Dynamics of Strike-Slip Step-Overs with Linking Dip-Slip Faults. *Bulletin of the Seismological Society of America*, 95(5):1604–1622, oct 2005. doi: 10.1785/0120050058.
- Power, W. L., Tullis, T. E., Brown, S. R., Boitnott, G. N., and Scholz, C. H. Roughness of natural fault surfaces. *Geophysical Research Letters*, 14(1):29–32, jan 1987. doi: https://doi.org/10.1029/GL014i001p00029.
- Romanet, P., Sato, D. S. K., and Ando, R. Curvature, a mechanical link between the geometrical complexities of a fault: application to bends, kinks and rough faults. *Geophysical Journal International*, 223(1):211–232, oct 2020. doi: 10.1093/gji/ggaa308.
- Sagy, A. and Brodsky, E. E. Geometric and rheological asperities in an exposed fault zone. *Journal of Geophysical Research: Solid Earth*, 114(B2), 2009. doi: 10.1029/2008JB005701.
- Sagy, A., Brodsky, E. E., and Axen, G. J. Evolution of fault-surface roughness with slip. *Geology*, 35(3):283–286, mar 2007. doi: 10.1130/G23235A.1.
- Schoenball, M. and Ellsworth, W. L. Waveform-Relocated Earthquake Catalog for Oklahoma and Southern Kansas Illuminates the Regional Fault Network. *Seismological Research Letters*, 88: 1252–1258, 7 2017.
- Shi, Z. and Day, S. M. Rupture dynamics and ground motion from 3-D rough-fault simulations. *Journal of Geophysical Research: Solid Earth*, 118(3):1122–1141, 2013. doi: 10.1002/jgrb.50094.
- Skoumal, R. J., Kaven, J. O., and Walter, J. I. Characterizing Seismogenic Fault Structures in Oklahoma Using a Relocated Template-Matched Catalog. *Seismological Research Letters*, 90: 1535–1543, 5 2019. doi: 10.1785/0220190045.
- Tal, Y., Hager, B. H., and Ampuero, J. P. The Effects of Fault Roughness on the Earthquake Nucleation Process. *Journal of Geophysical Research: Solid Earth*, 1 2018. doi: 10.1002/2017JB014746.

Tal, Y., Goebel, T., and Avouac, J.-P. Experimental and modeling study of the effect of fault roughness on dynamic frictional sliding. *Earth and Planetary Science Letters*, 536:116133, 2020. doi: <https://doi.org/10.1016/j.epsl.2020.116133>.

Tarnowski, J. M., Kyriakopoulos, C., Oglesby, D. D., Cooke, M. L., and Stern, A. The effects of pre-stress assumptions on dynamic rupture with complex fault geometry in the San Geronio Pass, California, region. *Geosphere*, 18(6):1710–1725, sep 2022. doi: [10.1130/GES02511.1](https://doi.org/10.1130/GES02511.1).

Thom, C. A., Brodsky, E. E., Carpick, R. W., Pharr, G. M., Oliver, W. C., and Goldsby, D. L. Nanoscale Roughness of Natural Fault Surfaces Controlled by Scale-Dependent Yield Strength. *Geophysical Research Letters*, 2017. doi: [10.1002/2017GL074663](https://doi.org/10.1002/2017GL074663).

Zielke, O., Galis, M., and Mai, P. M. Fault roughness and strength heterogeneity control earthquake size and stress drop. *Geophysical Research Letters*, 44:777–783, 2017. doi: [10.1002/2016GL071700](https://doi.org/10.1002/2016GL071700).

The article *Statistical distribution of static stress resolved onto geometrically-rough faults* © 2024 by Jeremy Maurer is licensed under CC BY 4.0.